



ORIGINAL ARTICLE

Controlled synthesis of 3D marigold-like ZnIn₂S₄/Ti₃C₂ for rapid and efficient removal of antibiotics



Ping Mao^{a,*}, Kun Liu^a, Aiwu Sun^{a,*}, Xin Yang^a, Xiaowu Ping^a, Jing Zhang^a, Jinyou Shen^b, Yuting Li^a, Jianfeng Teng^a, Yong Yang^{c,*}

^a National & Local Joint Engineering Research Center for Mineral Salt Deep Utilization, Key Laboratory for Palygorskite Science and Applied Technology of Jiangsu Province, School of Chemical Engineering, Huaiyin Institute of Technology, Huaian 223003, China

^b Jiangsu Key Laboratory of Chemical Pollution Control and Resources Reuse, School of Environmental and Biological Engineering, Nanjing University of Science and Technology, Nanjing 210094, China

^c Key Laboratory of Soft Chemistry and Functional Materials, Ministry of Education, School of Chemistry and Chemical Engineering, Nanjing University of Science and Technology, Nanjing 210094, China

Received 31 January 2023; accepted 2 April 2023

Available online 11 April 2023

KEYWORDS

Antibiotics;
3D marigold-like;
ZnIn₂S₄/Ti₃C₂;
Photocatalysis;
Synergistic effect

Abstract Developing of a rapid and efficient photocatalyst for the removal of antibiotics with high concentration in wastewater remediation is of great importance. 3D marigold-like ZnIn₂S₄/Ti₃C₂ was successfully fabricated by coupling 2D Ti₃C₂ nanosheets with hierarchical 3D ZnIn₂S₄ using a hydrothermal method. The degradation efficiency of ZnIn₂S₄/Ti₃C₂ composite for tetracycline (50 mg/L) and 7-Aminocephalosporanic acid (25 mg/L) within 120 min and 90 min can reach up to 91% and 95%, respectively. The introduction of Ti₃C₂ modulates the 3D marigold-like architecture of ZnIn₂S₄, which not only boosted its photon capture performance and adsorption capacity caused by the increased specific surface area, but also effectively separated photo-generated electrons and holes via the well-defined 2D/2D interface between ZnIn₂S₄ and Ti₃C₂. The synergistic effect of physical adsorption and photocatalytic degradation contributes to the high degradation efficiency and fast degradation performance. ZnIn₂S₄/Ti₃C₂ still exhibits high photocatalytic activity and excellent physicochemical stability after many cycles.

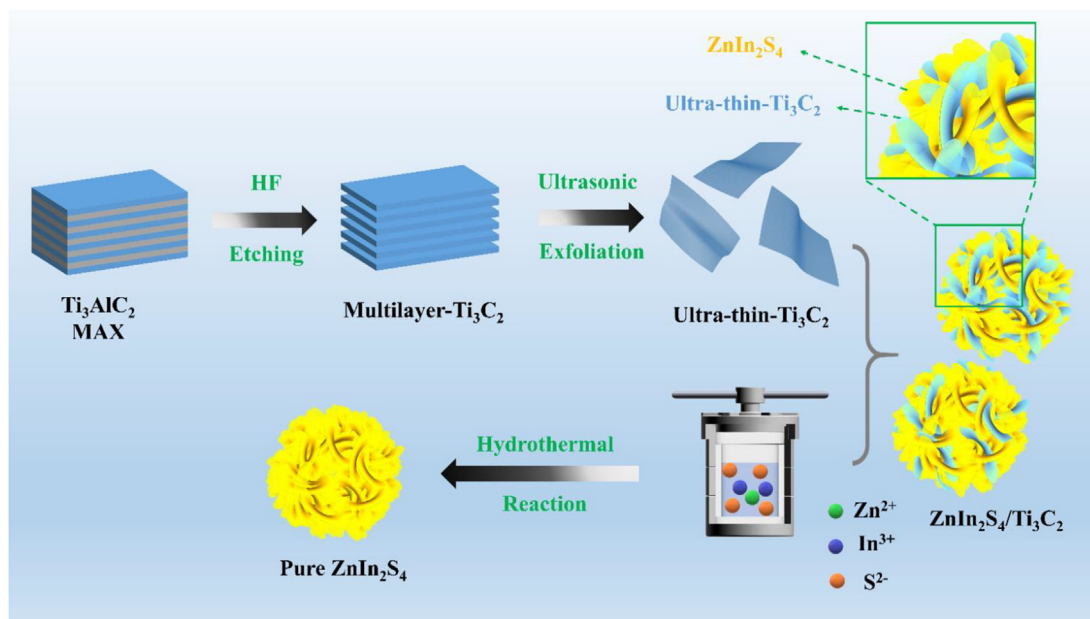
© 2023 The Author(s). Published by Elsevier B.V. on behalf of King Saud University. This is an open access article under the CC BY-NC-ND license (<http://creativecommons.org/licenses/by-nc-nd/4.0/>).

* Corresponding authors.

E-mail addresses: pingmao@hyit.edu.cn (P. Mao), sunaiwu@hyit.edu.cn (A. Sun), yychem@njjust.edu.cn (Y. Yang).

Peer review under responsibility of King Saud University.





Scheme 1 Schematic illustration of the fabrication process of pristine ZnIn₂S₄ and 3D marigold-like ZnIn₂S₄/Ti₃C₂.

several times. The resulting precipitates were dried in a vacuum oven at 60 °C for 12 h. MZ composites prepared with 3 mg, 6 mg, and 9 mg of Ti₃C₂ were named as MZ-3, MZ-6, and MZ-9, respectively. As a comparison, pure ZnIn₂S₄ was also prepared by the above method without Ti₃C₂.

2.3. Evaluation of photocatalytic activity

Firstly, 20 mg of the prepared sample was added into 100 mL of 50 mg/L tetracycline (TC) solution and 25 mg/L 7-Aminocephalosporanic acid (7-ACA) solution, respectively. The adsorption–desorption equilibrium was then obtained by stirring in the dark for 30 min. And then, the photodegradation reactions were performed by the visible light (300 W Xe lamp with a cut-off filter, $\lambda > 420$ nm). After a certain irradiation time, 5 mL of the suspension was taken out, and the photocatalyst was then removed with a 0.22 μ m filter before measurement. The absorbance of suspensions at 356 nm was measured by a Shimadzu UV2600 spectrophotometer at a certain interval to monitor the change of concentration of TC. The concentration of 7-ACA was determined by high-performance liquid chromatography (HPLC, APS80-16PLUS), which used an ultraviolet detector and an RP₁₈ column (dimension 4.6 \times 250 mm, 5.0 μ m), with sodium acetate-acetic acid buffer solution and acetonitrile (90:10, v/v) as effluent at a flow rate of 1.0 mL/min. The injection volume was 10 μ L. The degradation efficiency is calculated by Eq. (1).

$$\eta = (1 - c_t/c_0) \times 100\% \quad (1)$$

where η is photodegradation efficiency, c_0 is the initial concentration of adsorption–desorption equilibrium, and c_t is the remaining concentration, respectively.

To assess the stability of photocatalytic activity of the photocatalyst, the sample was collected by centrifugation after one test, washed with DI water several times and dried for the next cycle test.

3. Results and discussion

3.1. Characterization of all samples

The crystal structure of the Ti₃C₂, ZnIn₂S₄, and MZ composites was investigated by XRD analysis. As shown in Fig. S1, the most intense diffraction peak at 38.7° (2 θ) in the Ti₃AlC₂ pattern disappeared, and 9.6° allotted to the (002) plane of Ti₃C₂ moved to lower angles, indicating that Ti₃AlC₂ was successfully converted to Ti₃C₂ after etching treatment by HF (Alhabeib et al., 2017). XRD patterns of other samples are shown in Fig. 1a, the decreased peak intensity of the synthesized Ti₃C₂ indicated that the MAX powder lost its crystallinity after Al etching (Tariq et al., 2018). There are three strongly characteristic diffraction peaks at 21.6°, 27.7°, and 47.2°, corresponding to (006), (102), and (110) lattice planes of hexagonal ZnIn₂S₄ (JCPDS No.72–0773). After combination, the typical peaks of MZ composites are almost unchanged compared with that of the pristine ZnIn₂S₄, suggesting the excellent crystal structure of ZnIn₂S₄ is still maintained in MZ composites. However, no obvious Ti₃C₂ peaks can be found in the patterns of MZ composites owing to its low content (Cao et al., 2018).

To further study the recombination between ZnIn₂S₄ and Ti₃C₂, the surface element components and charge transfer in Ti₃C₂, ZnIn₂S₄, and MZ-6 were studied by XPS analyses. From the survey scan of the MZ-6 (Fig. 1b), the concomitant C, O, S, Ti, Zn, and In elements were detected. An obvious Ti peak could be seen through the high-resolution map of Ti 2p of MZ-6 (Fig. 1c), indicating the successful synthesis of ZnIn₂S₄/Ti₃C₂. And the peak showed a shift in relation to that in the pristine Ti₃C₂. Noticeable shift of bind energy was observed in the high-resolution XPS spectra of Zn 2p (Fig. 1d), suggesting that the electrons transfer from ZnIn₂S₄ to Ti₃C₂ in the Schottky junction, which indicates the close and robust interaction between Ti₃C₂ and ZnIn₂S₄. The Schottky junction

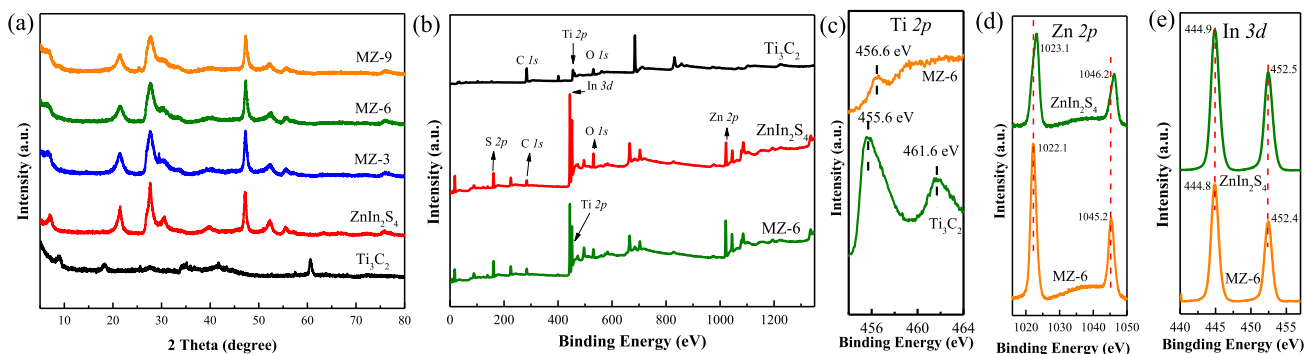


Fig. 1 (a) XRD patterns of Ti₃C₂, ZnIn₂S₄, MZ-3, MZ-6, MZ-9. (b) XPS survey spectra of Ti₃C₂, ZnIn₂S₄ and MZ-6. (c) Ti 2p, (d) Zn 2p, (e) In 3d core-level spectra of MZ-6, respectively.

can significantly improve the carrier separation rate and photocatalytic activity of sample (Ou et al., 2021).

FESEM and EDX measurements were used to analyze the morphology and composition of Ti₃AlC₂, multilayer Ti₃C₂, ultra-thin Ti₃C₂, pristine ZnIn₂S₄, and MZ-6 composite, respectively. The results are shown in Fig. 2, the original Ti₃AlC₂ is a bulk layered ternary carbide (Fig. 2a). After HF etching, accordion-like Ti₃C₂ is obtained (Fig. 2b). The few-layer ultrathin Ti₃C₂ nanosheets were then obtained by DMSO-intercalation assisted ultrasonic exfoliation (Fig. 2c). As shown

in Fig. 2d-f, pristine ZnIn₂S₄ is a 3D marigold-like hierarchical architecture assembled from a large number of nanosheets. The diameters of these assembled 3D ZnIn₂S₄ vary from 6 to 10 μm. Further observation shows that the nanosheets on the surface of these microspheres are incomplete and irregular. When Ti₃C₂ is introduced, 3D marigold-like hierarchical architecture does not change due to the small amount of Ti₃C₂. Interestingly, the diameter of the composite decreases significantly, but the nanosheets on the surface become more regular (Fig. 2g-i). Meanwhile, the elemental mapping of MZ-6 shown

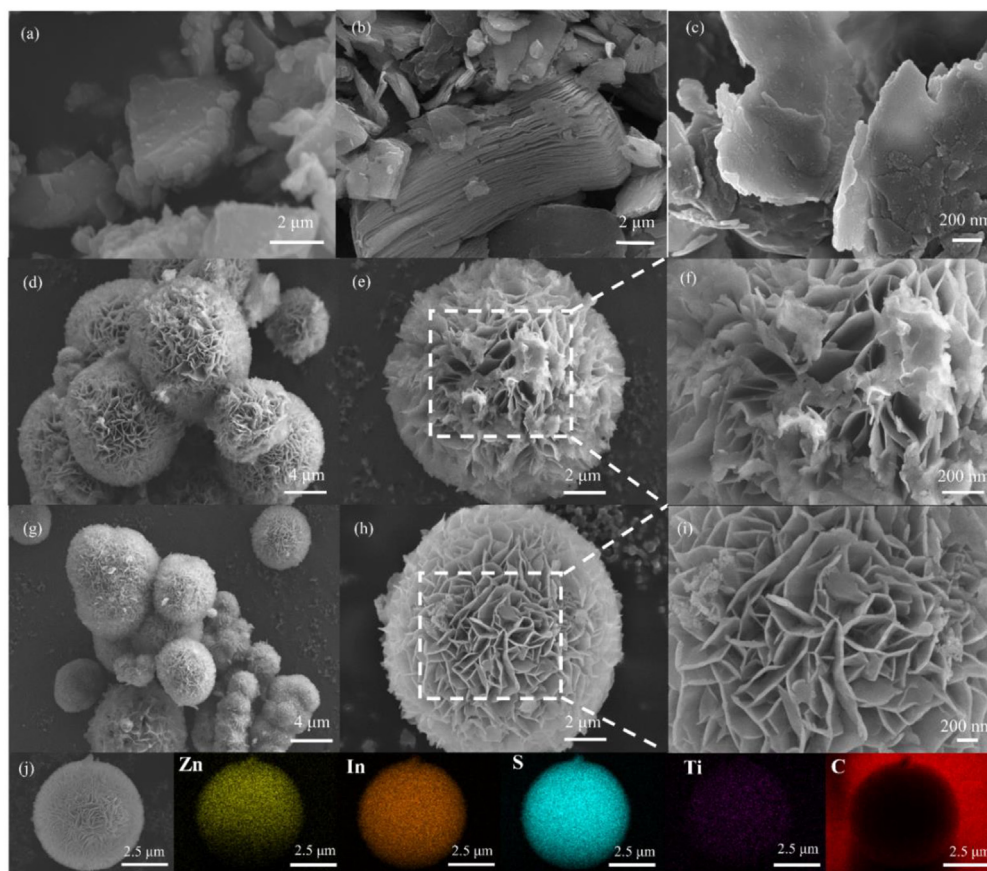


Fig. 2 FE-SEM images of (a) Ti₃AlC₂, (b) multilayer Ti₃C₂, (c) ultra-thin Ti₃C₂, (d-f) pristine ZnIn₂S₄ and (g-i) MZ-6. (j) EDX elemental mapping of MZ-6.

in Fig. 2j demonstrates that Zn, In, S, Ti, and C are uniformly distributed in the sample. The 2D nanosheets of Ti₃C₂ self-assemble and modify the hierarchical architecture of ZnIn₂S₄, which can give the sample a scattering cross section, and make it have good capability of antibiotics capture and photon trapping (Wang et al., 2021).

TEM characterization was then used to further discuss the morphology and internal structure of MZ-6. As well as SEM results, 3D structure with severe agglomeration can also be found in Fig. 3a, and the diameter of MZ-6 is around 2 μ m. HRTEM image shown in Fig. 2b also displays the spiny exterior of MZ-6. The clear lattice fringes with a spacing of 0.32, 0.22, and 0.26 nm belonged to ZnIn₂S₄ (102), ZnIn₂S₄ (108), and Ti₃C₂ (0110) can be observed from the magnified interface (Fig. 3c), successfully verifying the 2D/2D interface formed between ZnIn₂S₄ and Ti₃C₂, which can effectively facilitate the charge separation during photocatalysis. In view of the above characterizations, the possible construction mechanism of 3D marigold-like ZnIn₂S₄/Ti₃C₂ can be proposed. Zn²⁺ and In³⁺ in the solution were adsorbed on the negatively charged surface of Ti₃C₂. Then, in-situ hybridization of ZnIn₂S₄ on Ti₃C₂ nanosheets was simultaneously carried out by hydrothermal crystallization process, and the strong 2D/2D interface interaction between ZnIn₂S₄ and Ti₃C₂ was produced (Yang et al., 2019b). Afterwards, the 2D ZnIn₂S₄/Ti₃C₂ subunits were assembled to construct the well-defined 3D marigold-like hierarchical architecture (Wang et al., 2021).

To understand the light-harvesting capability of Ti₃C₂, ZnIn₂S₄, and MZ composites, ultraviolet–visible diffuse reflectance spectra were carried out. As shown in Fig. 4a, Ti₃C₂ exhibits a high absorption band in the visible region due to its dark color, the same as the previously reported work (Lukatskaya Maria et al., 2013). However, ZnIn₂S₄ gets a great improvement on the light absorption due to the introduction of Ti₃C₂. All MZ composites showed an obvious improvement of light absorption in the range of 450–800 nm, and with the increase of Ti₃C₂ content, the light absorption intensity of MZ composites increased slightly, suggesting the effective improvement of ZnIn₂S₄ light absorption through the Ti₃C₂ loading. The band gap values of ZnIn₂S₄, MZ-3 and MZ-6 can be calculated by the Tauc equation $(\alpha h\nu)^n = A(h\nu - E_g)$. The band gap value of ZnIn₂S₄ is estimated to be 2.36 eV (Fig. 4b). The band gap becomes narrower after the addition of Ti₃C₂. The values of the band gap energy of MZ-3 and MZ-6 were 2.33 eV and 2.27 eV, respectively. Moreover, the exact conductive band (CB) potential of MZ-6 was calculated to be -0.90 V ($E_{NHE} = E_{Ag/AgCl} + 0.197$ (V)) by Mott-

Schottky measurement. Thus, the valence band (VB) of ZnIn₂S₄ is 1.37 V.

The surface-active site is an essential factor affecting photocatalytic degradation efficiency. Therefore, the specific surface areas and pore sizes of Ti₃C₂, ZnIn₂S₄, and MZ composites were determined. As shown in Fig. 4c. Ti₃C₂ has a typically reversible microporous adsorption curve (type I curves), indicating that the material is mainly composed of micropores (Sun et al., 2020). Both ZnIn₂S₄ and MZ composites exhibit IV-type adsorption with the H-3 type hysteresis loops, which implied that mesoporous structures are occur in these samples. Meanwhile, the specific surface area of Ti₃C₂, ZnIn₂S₄, MZ-6, and MZ-9 was 4.67, 43.27, 71.46, and 34.9 m²/g, respectively. MZ-6 has the highest specific surface area due to the well-defined 3D hierarchical architecture. However, excess of Ti₃C₂ in MZ-9 leads to the agglomeration of the components, thus the specific surface area of MZ-9 is unambiguous decreased. Higher specific surface area is conducive to the formation of more surface active sites, and strengthens the photon capture, which can enhance photocatalytic activity (Xiao et al., 2018). Fig. 4d shows the pore size distribution curves of the samples. The distribution of pore size for ZnIn₂S₄ and MZ-6 is mainly below 5 nm. Combined with the previous SEM results, the well-defined 3D hierarchical architecture initiated by introduction of Ti₃C₂ is helpful for the formation of mesoporous and the increase in specific surface areas. Thus, MZ-6 is expected to be the most promising photocatalyst.

3.2. Photocatalytic measurement

To investigate the photocatalytic activities of Ti₃C₂, ZnIn₂S₄, and MZ composites on antibiotics under visible light irradiation, the photocatalytic degradation of TC and 7-ACA was assessed. In order to test the stability of all samples, blank tests were used to check for metal leakage from the samples and the content of related metals was detected by ICP. No Zn, Ti and other metals were detected, indicating good stability of all samples. The degradation efficiencies of all samples for TC are shown in Fig. 5a. The concentration of TC is not varied in the blank experiment, implying that TC possess high stability. In addition, Ti₃C₂ barely exhibits a degradation effect on TC. However, the photocatalytic degradation efficiency of pristine ZnIn₂S₄ is about 70.2%. Moreover, the photocatalytic efficiency of MZ composites is significantly improved after incorporation with Ti₃C₂. MZ-3 exhibits a degradation efficiency of approximately 86%. MZ-6 shows the optimum photocatalytic degradation, its degradation efficiency for TC can reach up to

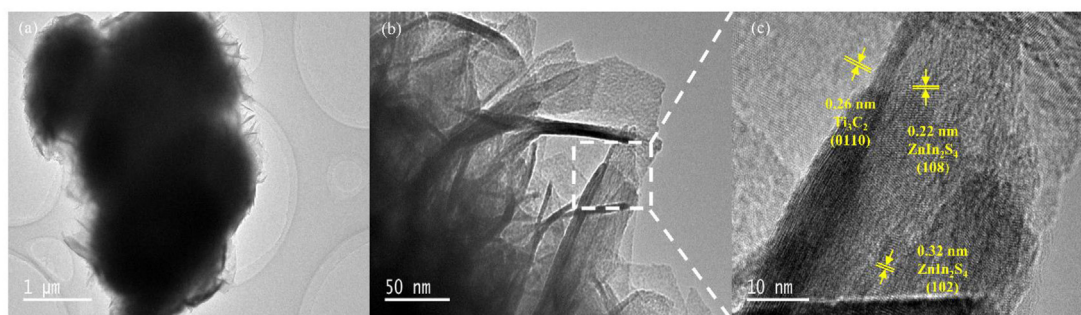


Fig. 3 TEM (a, b) images of the MZ-6 and HRTEM of the enlarged area of the block (c).

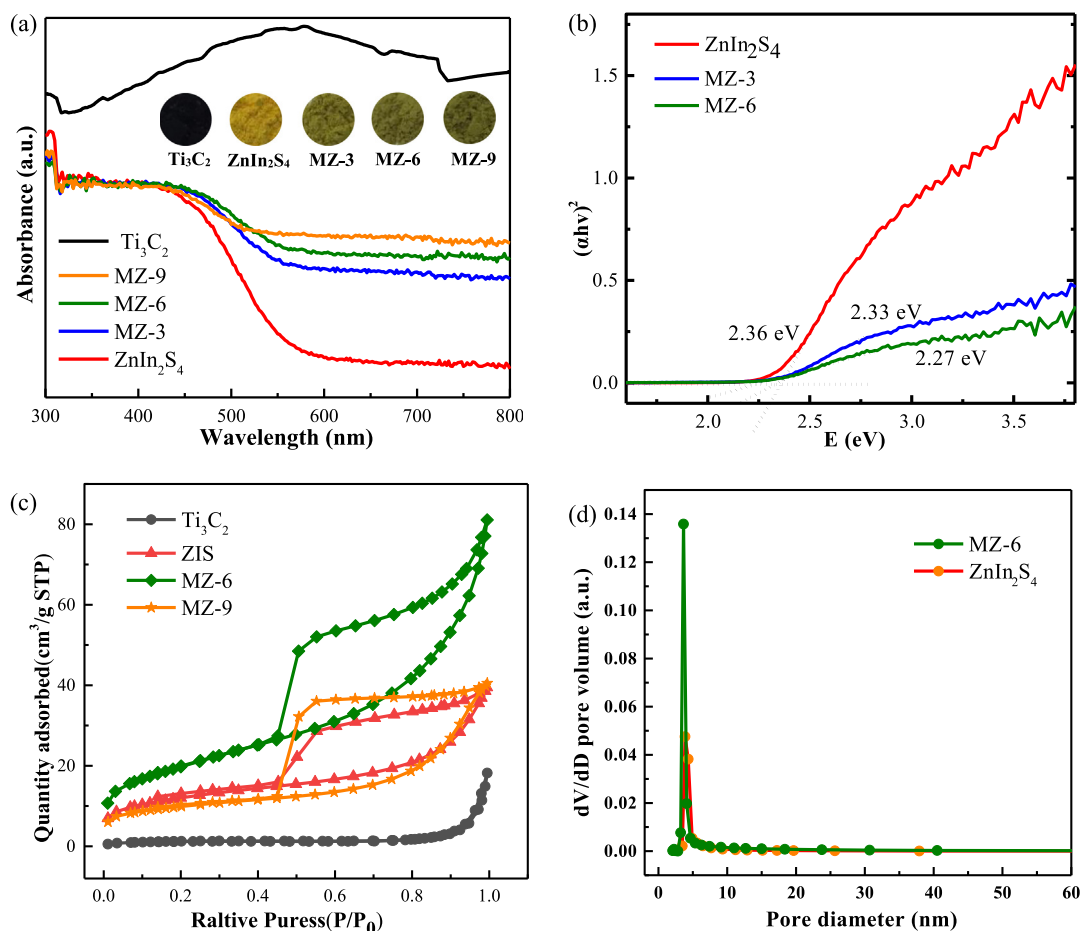


Fig. 4 (a) UV-vis diffuse reflectance spectra (DRS) of Ti_3C_2 , ZnIn_2S_4 and MZ composites (digital pictures). (b) The band gap of ZnIn_2S_4 . (c) N_2 adsorption-desorption isotherms and (d) pore size distribution of Ti_3C_2 , ZnIn_2S_4 and MZ-6 at 77K.

91% after 2 h of visible-light irradiation. Unfortunately, the photocatalytic degradation efficiency of MZ-9 only has 82%. Clearly, the introduction of Ti_3C_2 can effectively improve the photocatalytic activity of ZnIn_2S_4 , but there is an optimal ratio between ZnIn_2S_4 and Ti_3C_2 . Besides TC, 7-ACA was also degraded under visible light. The result is shown in Fig. 5b, 7-ACA also possess high stability under visible light irradiation. As was the case with the TC, all MZ composites are more efficient than pristine ZnIn_2S_4 . Similarly, after 90 min of visible light irradiation, MZ-6 shows the best degradation efficiency on 7-ACA, which can reach up to 95%.

Furthermore, the experiments were quantitatively explained by the pseudo-first-order reaction kinetics equation. The results are shown in Fig. S4a and Fig. S4b, MZ-6 shows the highest photocatalytic activity for TC ($k = 0.01947 \text{ min}^{-1}$) and 7-ACA ($k = 0.02999 \text{ min}^{-1}$). The above results indicate that MZ-6 is an effective photocatalyst for the degradation of different antibiotics.

Besides photocatalytic activities, the adsorption activities of all samples were also investigated. As shown in Fig. S3, the adsorption-desorption equilibrium of all samples for TC and 7-ACA can be reached within 30 min. Meanwhile, among all the samples, MZ-6 exhibits the best adsorption capacity for TC and 7-ACA, which can achieve 29.4% and 14.5%, respectively. Ti_3C_2 has barely adsorption capacity, and ZnIn_2S_4 only

reached 11.7% and 8.4%. Similarly, the trend of the adsorption activities of all samples are in consist with their BET specific surface areas, indicating that the BET specific surface areas and the well-defined pores distribution play fundamental roles in their adsorption performance. Consequently, the reason why MZ-6 has the superior degradation performance: MZ-6 possesses higher specific surface area, which not only provides more transmission paths and improves the absorption and utilization of visible light, but also enriched the surrounding concentration of antibiotics. Afterwards, the instruction of Ti_3C_2 has a positive promoting effect for the photocatalytic degradation of ZnIn_2S_4 . Unfortunately, the further increase of Ti_3C_2 results in severe agglomeration in MZ-9, which significantly decrease its exposure of active sites and photodegradation performances.

To further analyze the advantages of photocatalytic performance of MZ-6, the photocatalytic degradation of MZ-6 for TC and 7-ACA was compared with other similar photocatalysts reported in the literatures. As shown in Table 1. MZ-6 still has good 91% and 95% degradation efficiency for 50 mg/L of TC and 25-mg/L of 7-ACA, and the degradation velocity reaches 113.8 mg/g-h and 59.4 mg/g-h, which is 1.5 and 14.8 times higher than other photocatalysts, respectively. It is obvious that MZ-6 exhibits a highest photocatalytic degradation performance. This result further indicated that

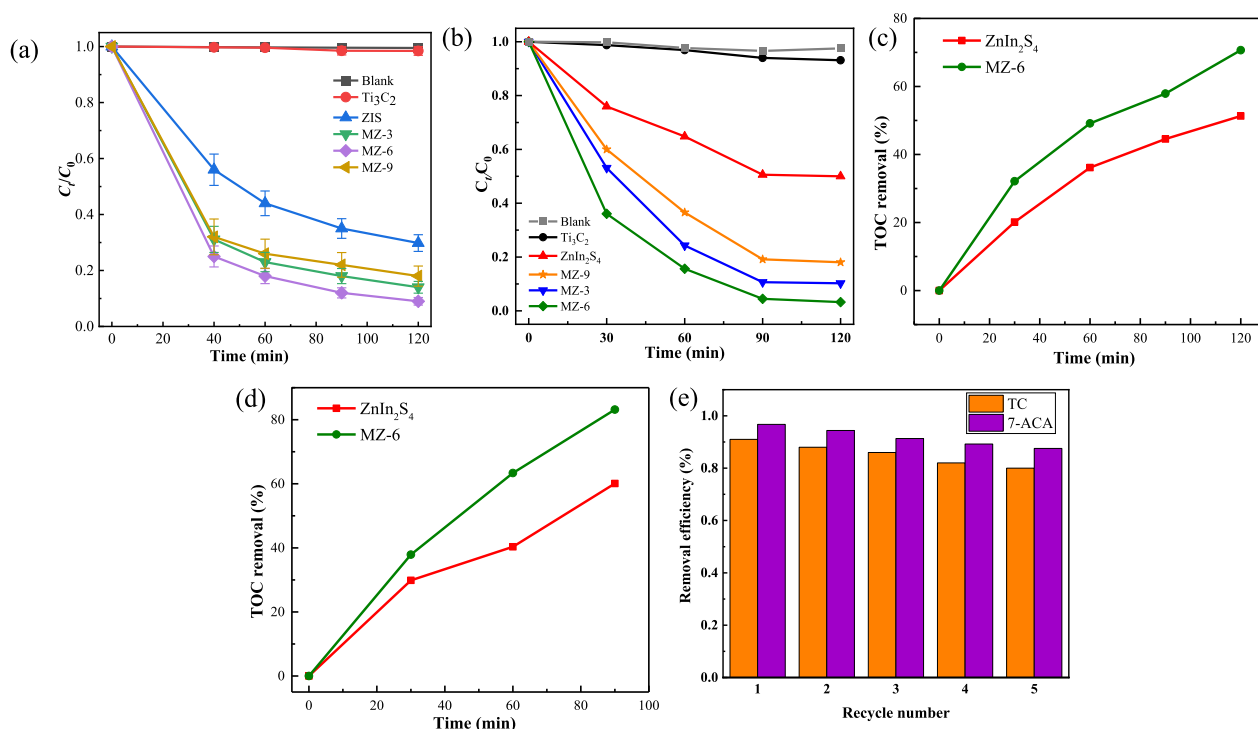


Fig. 5 Photocatalytic degradation of TC (a) and 7-ACA (b) by samples under visible light irradiation. TOC removal curve of TC (c) and 7-ACA (d) in the presence of pristine ZnIn₂S₄ and MZ-6 under visible light irradiation. (e) Photocatalytic degradation of TC and 7-ACA in solution for 5 cycles using MZ-6 under visible light irradiation.

Table 1 Comparison of the photocatalytic degradation of TC and 7-ACA by different photocatalysts.

photocatalyst	Dosage (mg)	Antibiotics (mg/L)	Volume (mL)	Solid-to-liquid Ratio (g/L)	Photocatalytic Efficiency/Time	Degradation Velocity (mg/g·h)	Ref
TiO ₂ /ZnIn ₂ S ₄	10	TC (20)	50	0.20	95.1%/120 min	47.6	(Liu et al., 2021)
CeO ₂ /ZnIn ₂ S ₄	10	TC (30)	50	0.20	91%/120 min	68.3	(Hao et al., 2021)
ZnIn ₂ S ₄ /BiPO	15	TC (40)	50	0.30	84%/90 min	74.7	(Lu et al., 2019)
ZnIn ₂ S ₄ /Ta ₃ N ₅	20	TC (15)	60	0.33	89.95%/180 min	13.5	(Xiao et al., 2020)
ZnIn ₂ S ₄ /(CQDs)	20	TC (10)	80	0.25	85.07%/240 min	8.5	(Xu et al., 2018)
MZ-6	20	TC (50)	100	0.10	91%/120 min	113.8	This work
Ag-CsPbBr ₃ /CN	100	7-ACA (10)	100	1.00	92.79%/140 min	4.0	(Zhao et al., 2019)
MZ-6	20	7-ACA (25)	100	0.20	95%/120 min	59.4	This work

MZ-6 could be considered as a promising photocatalyst for the degradation of antibiotics.

To understand whether the antibiotics were removed in the form of mineralization or conversion to other organic compounds during photocatalysis, the total organic carbon (TOC) of degradation products was detected. The results of the TOC removal rates of TC and 7-ACA by photocatalysts are shown in Fig. 5c and d. As it can be seen, the TOC removal rates were lower than the degradation efficiencies during photocatalysis. But the trend of the TOC removal rate is similar to that of the photocatalytic degradation curve. This is because there are still small quantities of intermediates in the solution that have not been wholly converted to inorganic substances (Lu et al., 2019). Nevertheless, compared with the pristine ZnIn₂S₄, the mineralization capacity of MZ-6 is demonstrated to be significantly improved.

It's very important to study the reusability of the photocatalyst in practical application. To this end, the stability and reusability experiments were investigated. The photocatalytic activity of MZ-6 only declines about 14.4% (for TC) and 11.2% (for 7-ACA) after 5 cycles (Fig. 5e), indicating that MZ-6 possess an outstanding stability through the whole photocatalytic degradation process. The XRD patterns of MZ-6 before and after the photocatalytic reaction are shown in Fig. S5, no obvious change in crystal structure was observed. SEM and TEM images (Fig. S6) of MZ-6 after the photo degradation showed that the 3d marigold like structure did not change greatly, but there were some larger holes in some spheres, which might be caused by the loss of some crystals because of the repeated use, and this was the main reason for the slight decline in photocatalytic performance of MZ-6. The unchanged structure of the photocatalyst further proves

that the photocatalyst has good chemical stability. In conclusion, MZ-6 exhibits well-maintained degradation efficiency, excellent stability and high practical application potential.

The effect of different pH values on the degradation were explored. The result was clearly seen from Fig. 6a, the adsorption efficiency of MZ-6 on TC reached 36% at pH = 3.5, and decreased with the increase of pH value, indicating that MZ-6 showed excellent adsorption properties under acidic conditions. The change of TC overall removal by MZ-6 was also same, which may be caused by the electrostatic interaction between TC and MZ-6. As we know, TC is an amphoteric compound with multiple ionizing functional groups, and behaves in different forms under different pH conditions: positive ions (TCH_3^+) (acidity), zwitterions (TCH_2^0) (neutral), and negative ions ($\text{TCH}^-/\text{TC}_2^-$) (alkalinity)(Xiang et al., 2020). Meanwhile, the surface of ZIS was positively charged when $\text{pH} < 2.4$ and negatively charged when $\text{pH} > 2.4$ (Luo et al., 2022). Therefore, a stronger electrostatic attraction between positively charged TC and negatively charged MZ-6 under acidic condition, which promoted the adsorption of TC. And the electrostatic repulsion was produced under alkaline condition. However, the better stability and the smaller particle size of the prepared samples also accelerated the separation of photo-generated electron-hole pairs, resulting in more active sites of contact between the catalyst and TC, thus the superior removal efficiency of TC in wide pH range could be achieved by MZ-6. In addition, the effect of pH on 7-ACA was clearly seen from Fig. 6b, the enhanced removal of 7-ACA was achieved both acidic and alkaline conditions. This phenomenon could be caused by the decomposition of 7-ACA (Sahoo et al. 1996).

3.3. Mechanism considerations

The recombination process of the photoexcited electron-hole pairs is usually illustrated by the photoluminescence (PL) spectroscopy (Chen et al., 2017). Photocatalysts produce electron-hole pairs under light irradiation. And then, the photoinduced carrier migrates to the surface of the photocatalyst for a redox reaction. The combination of electrons and holes produces a fluorescence signal that can be observed by photoluminescence spectra. In general, the higher photoluminescence intensity is, the more severe recombination of photo-generated electron-hole pairs is (Wang et al., 2016b). Herein, the fluorescence spectra of pristine ZnIn_2S_4 , MZ-3, and MZ-6 series composites were determined by PL. As shown in Fig. 6c, owing to the band gap recombination of photo-generated electrons and holes, a broad peak or pristine ZnIn_2S_4 is observed near 468 nm. The fluorescence intensity of all MZ composites is lower than that of ZnIn_2S_4 , suggesting that the hybridization of Ti_3C_2 nanosheets with ZnIn_2S_4 can significantly reduce the electron-hole pairs recombination, which further indicates that the photocatalytic activities of MZ composites are improved.

To further investigate the spatial separation and transfer of the charge carriers in photocatalysis, photoelectrochemical tests were carried out (Tan et al., 2019). The electronic conductivity and the charge carrier transfer capacity of photocatalysis can be evaluated by the transient photocurrent response curves and electrochemical impedance spectra (EIS) (Yang et al., 2018). The results of transient photocurrent response of ZnIn_2S_4 and MZ composites under intermittent solar simulator irradiation are shown in Fig. 6d. The positive photocurrent curve

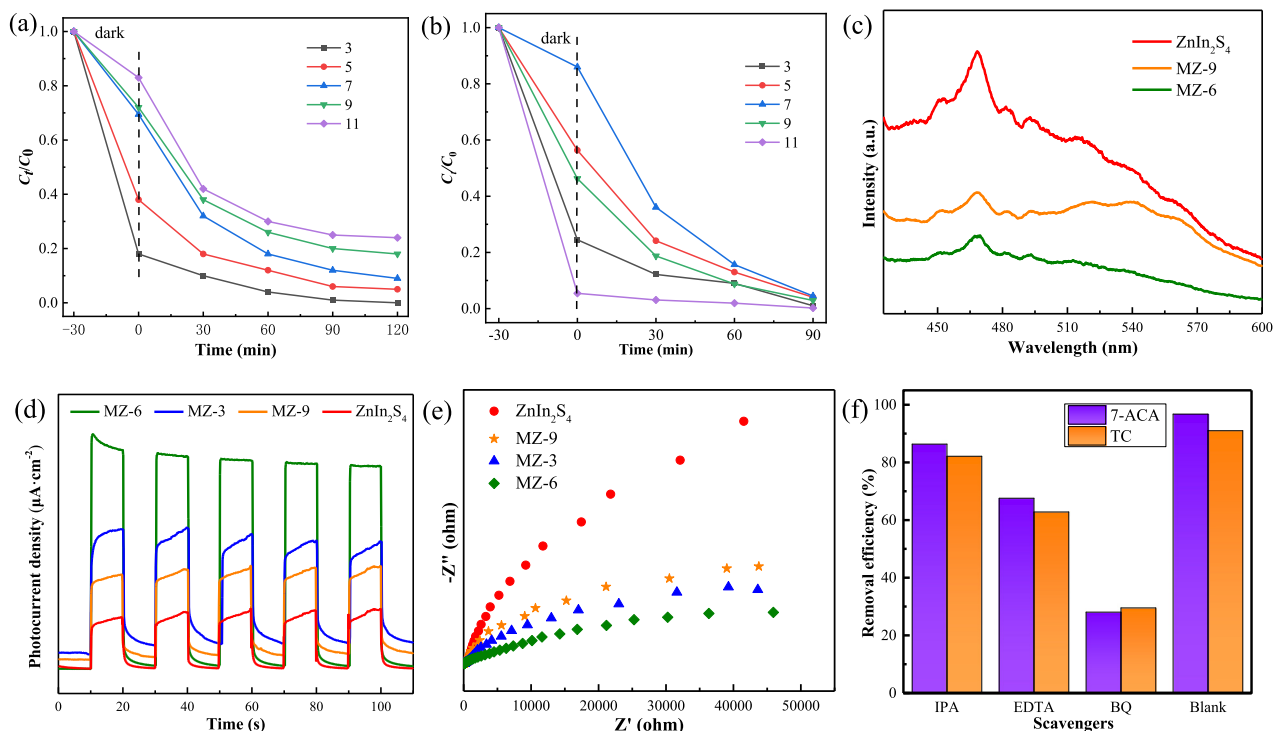


Fig. 6 Photocatalytic degradation of TC (a) and 7-ACA (b) over different pH. (c) PL spectra of ZnIn_2S_4 , MZ-6 and MZ-9. Transient photocurrent responses (d) and EIS (e) of ZnIn_2S_4 and MZ composites. (f) Trapping experiment of active species during the photodegradation of TC and 7-ACA.

of ZnIn₂S₄ shows that it is an n-type semiconductor. The photocurrent density increases rapidly and reaches saturation when the light is bright, but as soon as the light is turned off, it immediately drops to nearly zero. Moreover, the photocurrent intensity of ZnIn₂S₄ increased after the modification of Ti₃C₂, but there is an optimized ratio between ZnIn₂S₄ and Ti₃C₂, and MZ-6 shows the highest photocurrent response. The rise of photocurrent confirmed that MZ-6 Schottky junction can promote the separation of photocarriers, prolong the life of photocarriers, improve the absorption of visible light, and then promote the enhancement of photocatalytic activity. However, excessive Ti₃C₂ in MZ-9 results in a decrease in photocurrent intensity, which may be caused by strong light absorption of Ti₃C₂ and agglomeration of components. In general, the smaller the semicircle diameter of the Nyquist diagram is, the smaller the charge transfer resistance of photocatalyst is. An arc radius per sample can be observed in Fig. 6e, suggesting that only surface charge-transfer mode occurred during photocatalysis. The smaller the semicircle diameter of the Nyquist diagram of MZ-6 confirms the contribution of a 2D/2D interface to conductivity. In comparison to ZnIn₂S₄, it is demonstrated that the electronic conductivity of MZ-6 is higher due to electron transfer between ZnIn₂S₄ and Ti₃C₂. The lowest charge transfer resistance and highest electronic conductivity facilitate the most efficient charge separation for MZ-6. This is consistent with its significantly enhanced photocatalytic activity.

Generally, hydroxyl radical ($\cdot\text{OH}$), superoxide radical ($\cdot\text{O}_2^-$), and hole (h^+) are three typical active substances for pollutant degradation. To study the role of each active substance during photocatalysis of MZ composites, corresponding masking agent was introduced to investigate the change of degradation activity of MZ-6 for TC and 7-ACA under visible light. In these experiments, the masking agents used to eliminate $\cdot\text{OH}$, $\cdot\text{O}_2^-$, and h^+ were isopropanol (IPA), benzoquinone (BQ), and ethylenediaminetetraacetic acid (EDTA), respectively. The result is shown in Fig. 6f, the degradation efficiency of MZ-6 for TC (7-ACA) decreased from 91% (96.75%) to 82.12% (86.34%), 29.52% (28.06%), and 62.82% (67.57%)

when IPA, BQ and EDTA were added, respectively. It indicates that $\cdot\text{O}_2^-$ and h^+ are the major active substances in the degradation of TC. Moreover, the pH values during the trapping agent experiment were detected. The result is shown in Fig. S7, the initial pH of the solution was different due to the masking agent. The pH of the solution containing IPA and EDTA decreased gradually with the increase of light time, but the solution containing BQ was the opposite. Combined their degradation efficiencies' showed that this is mainly caused by the degradation and intermediates product (CO_2).

To better understand the photocatalytic degradation of MZ composites for 7-ACA and TC, the intermediates were identified by LC-MS and HPLC-MS experiments. Similar to previous studies (Zhao et al., 2019), three typical species with the value of m/z at 231, 229, and 146 can be observed in Fig. S8. As illustrated in Fig. S9, we propose two different pathways to degrade 7-ACA according to these typical species. In the first reaction pathway, since β -lactam antibiotics are prone to ring-opening reactions (Lima et al., 2020), the structure A (7-ACA, $m/z = 272.05$) can be degraded to the structure B ($m/z = 231.04$) with the ring-opening reactions of β -lactam. As the degradation continues, structure C ($m/z = 145.04$) will be degraded from structure B. And then, structure C converts to CO_2 and H_2O . In another reaction pathway, the $-\text{COOH}$ group falls off from structure A (7-ACA, $m/z = 272.05$) to generate the intermediate D ($m/z = 229.06$). And with prolonged illumination, all intermediates tend to convert to CO_2 and H_2O . As shown in Fig. S10 and Fig. S11, The m/z of TC is 445, two possible TC degradation pathways were analyzed. In pathway I, TC firstly produce structure B ($m/z = 417$) through N-dealkylation reaction. Then h^+ attacked electron-rich $\text{C}1 = \text{C}18$, resulting in structure C ($m/z = 393$), structure B and structure C could further transform during photocatalytic oxidation to form structure D ($m/z = 349$). Subsequently, structure E ($m/z = 279$) was generated by decarboxylation and ring-opening reaction. In pathway II, TC was demethylated to form structure F ($m/z = 431$). Afterwards, structure F was further converted to structure G ($m/z = 398$) by losing amino groups and H_2O . Then, structure

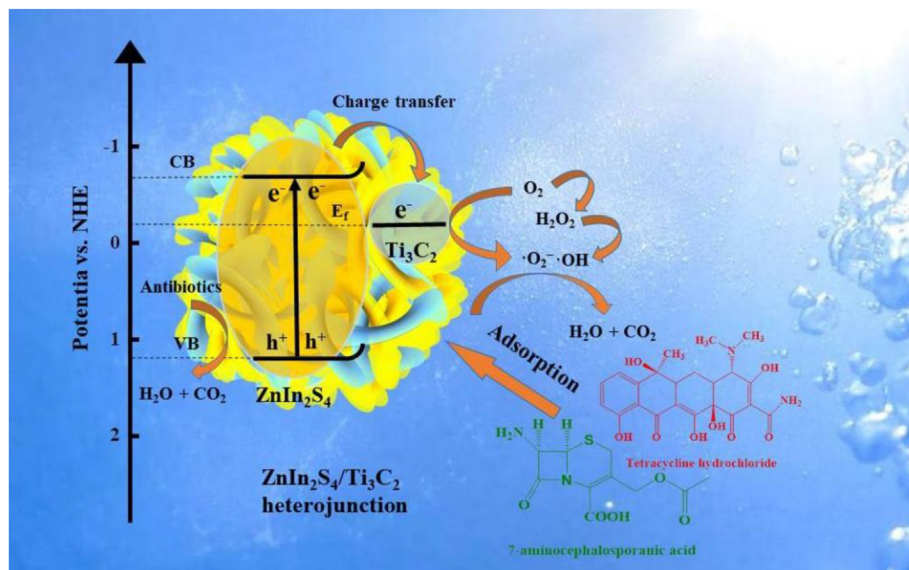
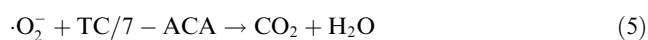
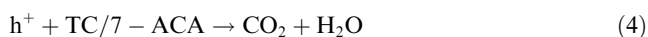


Fig. 7 The mechanism of photodegradation and photoreduction of MZ-6.

H ($m/z = 284$) was generated after losing aldehyde groups and benzene ring-opening reaction. Ultimately, these intermediates could be further decomposed into smaller non-polar molecular materials, even CO_2 and H_2O (Li et al., 2022).

On this basis, the possible photodegradation mechanism of MZ composites was proposed. Firstly, $\text{ZnIn}_2\text{S}_4/\text{Ti}_3\text{C}_2$, which has a large specific surface area of 3D marigold-like structure, enrich antibiotics in its surrounding area via physical adsorption, so that the concentration of antibiotics around it is relatively high. Secondly, under the irradiation of visible light, the high specific surface area provides more transmission paths for visible light. As shown in Fig. 7, photogenerated electrons are excited from VB of ZnIn_2S_4 to CB. Since the CB potential of ZnIn_2S_4 is lower than the Fermi level of Ti_3C_2 , photogenerated electrons will be transferred to Ti_3C_2 through the 2D/2D interface between ZnIn_2S_4 and Ti_3C_2 . Meanwhile, the in-situ $\text{ZnIn}_2\text{S}_4/\text{Ti}_3\text{C}_2$ composite facilitates the close contact with each other, greatly improves the interface charge migration and photoinduced electron-hole pair separation, promotes the electron capture of Ti_3C_2 , and significantly reduces the electron-hole pair recombination. In addition, the Fermi energy levels of ZnIn_2S_4 and Ti_3C_2 are lower than the potential of $\text{O}_2/\cdot\text{O}_2^-$, the electrons that accumulate on Ti_3C_2 can be rapidly transferred to the surface to participate in the formation of $\cdot\text{O}_2^-$, giving it strong oxidation properties. Finally, TC and 7-ACA can be degraded by $\cdot\text{O}_2^-$ and h^+ . The reactions were described as follows:



4. Conclusion

In summary, well-defined 3D marigold-like MZ composites had been successfully prepared by a simple hydrothermal method. The introduction of Ti_3C_2 ameliorates the disadvantage of sulfides being easy to photocorroded by light to some extent. These composites exhibit outstanding photocatalytic activity. The optimized MZ-6 composite possess the best photocatalytic degradation and adsorption activity for antibiotics, and the removal efficiency of TC and 7-ACA exceeded 90% in a short time. Importantly, MZ still has excellent physical and chemical stability and high photocatalytic activity after multiple cycles. In addition, $\cdot\text{O}_2^-$ and h^+ play a major role in the degradation of antibiotics. This study further confirms that Ti_3C_2 can be used as a co-catalyst to broaden its application in rapid and efficient photocatalysis.

Declaration of competing interest

The authors declare that they have no known competing financial interests or personal relationships that could have appeared to influence the work reported in this paper.

Acknowledgments

This work was supported by the National Natural Science Foundation of China (No. 51908240), the Natural Science Foundation of Jiangsu Province (No. BK20181064), the Nat-

ural Science Research of Jiangsu Higher Education Institutions of China (No. 18KJB610003), Qing Lan Project, the Postgraduate Research & Practice Innovation Program of Jiangsu Province (No. SJCX21_1499), the Foundation of Jiangsu Provincial Key Laboratory of Palygorskite Science and Applied Technology (No. HPK201905).

Appendix A. Supplementary material

Supplementary data to this article can be found online at <https://doi.org/10.1016/j.arabjc.2023.104883>.

References

- Abdul Mubarak, N.S., Foo, K.Y., Schneider, R., Abdelhameed, R.M., Sabar, S., 2022. The chemistry of MIL-125 based materials: Structure, synthesis, modification strategies and photocatalytic applications. *J. Environ. Chem. Eng.* 10, (1) 106883.
- Ahmed, M.B., Zhou, J.L., Ngo, H.H., Guo, W., 2015. Adsorptive removal of antibiotics from water and wastewater: Progress and challenges. *Sci. Total Environ.* 532, 112–126.
- Alhabeab, M., Maleski, K., Anasori, B., Lelyukh, P., Clark, L., Sin, S., Gogotsi, Y., 2017. Guidelines for synthesis and processing of two-dimensional titanium carbide ($\text{Ti}_3\text{C}_2\text{T}_x$ MXene). *Chem. Mater.* 29 (18), 7633–7644.
- Cai, T., Wang, L., Liu, Y., Zhang, S., Dong, W., Chen, H., Yi, X., Yuan, J., Xia, X., Liu, C., Luo, S., 2018. $\text{Ag}_3\text{PO}_4/\text{Ti}_3\text{C}_2$ MXene interface materials as a Schottky catalyst with enhanced photocatalytic activities and anti-photocorrosion performance. *Appl. Catal. B* 239, 545–554.
- Cao, S., Shen, B., Tong, T., Fu, J., Yu, J., 2018. 2D/2D heterojunction of ultrathin MXene/ Bi_2WO_6 nanosheets for improved photocatalytic CO_2 reduction. *Adv. Funct. Mater.* 28 (21), 1800136.
- Chen, G., Ding, N., Li, F., Fan, Y., Luo, Y., Li, D., Meng, Q., 2014. Enhancement of photocatalytic H_2 evolution on ZnIn_2S_4 loaded with in-situ photo-deposited MoS_2 under visible light irradiation. *Appl. Catal. B* 160–161, 614–620.
- Chen, S., Yan, R., Zhang, X., Hu, K., Li, Z., Humayun, M., Qu, Y., Jing, L., 2017. Photogenerated electron modulation to dominantly induce efficient 2,4-dichlorophenol degradation on BiOBr nanoplates with different phosphate modification. *Appl. Catal. B* 209, 320–328.
- Cheng, L., Chen, Q., Li, J., Liu, H., 2020. Boosting the photocatalytic activity of CdLa_2S_4 for hydrogen production using Ti_3C_2 MXene as a co-catalyst. *Appl. Catal. B* 267, 118379.
- Deng, Y., 2020. Low-cost adsorbents for urban stormwater pollution control. *Front. Environ. Sci. Eng.* 14 (5), 83.
- Ding, L., Wei, Y., Wang, Y., Chen, H., Caro, J., Wang, H., 2017. A Two-dimensional lamellar membrane: MXene nanosheet stacks. *Angew. Chem. Int. Ed.* 56 (7), 1825–1829.
- Gao, Y., Li, Y., Zhang, L., Huang, H., Hu, J., Shah, S.M., Su, X., 2012. Adsorption and removal of tetracycline antibiotics from aqueous solution by graphene oxide. *J. Colloid Interface Sci.* 368 (1), 540–546.
- Gao, B., Safaei, Z., Babu, I., Iftekhar, S., Iakovleva, E., Srivastava, V., Doshi, B., Hammouda, S.B., Kalliola, S., Sillanpää, M., 2017. Modification of ZnIn_2S_4 by anthraquinone-2-sulfonate doped polypyrrole as acceptor-donor system for enhanced photocatalytic degradation of tetracycline. *J. Photochem. Photobiol. A Chem.* 348, 150–160.
- Guo, Y., Xin, C., Dai, L., Zhang, Y., Yu, X., Guo, Q., 2022a. Layered and porous (Al , C)- T_aO_5 mesocrystals supported CdS quantum dots for high-efficiency photodegradation of organic contaminants. *Sep. Purif. Technol.* 284, 120297.
- Guo, Y.N., Zhang, D., Wang, M., Wei, G., Nie, Z., Yang, X., Li, Z., Zhang, Y., Peng, Y., 2022b. Synergistic modulation on atomic-level

- 2D/2D Ti₃C₂/Svac-ZnIn₂S₄ heterojunction for photocatalytic H₂ production. *Colloids Surf. A: Physicochem. Eng. Aspects* 648.
- Hao, C.-C., Tang, Y.-B., Shi, W.-L., Chen, F.-Y., Guo, F., 2021. Facile solvothermal synthesis of a Z-Scheme 0D/3D CeO₂/ZnIn₂S₄ heterojunction with enhanced photocatalytic performance under visible light irradiation. *Chem. Eng. J.* 409, 128168.
- Hong Ng, V.M., Huang, H., Zhou, K., Lee, P.S., Que, W., Xu, Z.J., Kong, L.B., 2017. Correction: Recent progress in layered transition metal carbides and/or nitrides (MXenes) and their composites: synthesis and applications. *J. Mater. Chem. A* 5 (18), 8769.
- Huang, Y., Li, H., Balogun, M.-S., Liu, W., Tong, Y., Lu, X., Ji, H., 2014. Oxygen vacancy induced bismuth oxyiodide with remarkably increased visible-light absorption and superior photocatalytic performance. *ACS Appl. Mater. Interfaces* 6 (24), 22920–22927.
- Huang, Y., Long, B., Tang, M., Rui, Z., Balogun, M.-S., Tong, Y., Ji, H., 2016a. Bifunctional catalytic material: An ultrastable and high-performance surface defect CeO₂ nanosheets for formaldehyde thermal oxidation and photocatalytic oxidation. *Appl. Catal. B* 181, 779–787.
- Huang, Y., Fan, W., Long, B., Li, H., Zhao, F., Liu, Z., Tong, Y., Ji, H., 2016b. Visible light Bi₂S₃/Bi₂O₃/Bi₂O₂CO₃ photocatalyst for effective degradation of organic pollutions. *Appl. Catal. B* 185, 68–76.
- Huang, Y., Guo, Z., Liu, H., Zhang, S., Wang, P., Lu, J., Tong, Y., 2019. Heterojunction architecture of N-doped WO₃ nanobundles with Ce₂S₃ nanodots hybridized on a carbon textile enables a highly efficient flexible photocatalyst. *Adv. Funct. Mater.* 29 (45), 1903490.
- Jing, D., Liu, M., Guo, L., 2010. Enhanced hydrogen production from water over Ni doped ZnIn₂S₄ microsphere photocatalysts. *Catal. Lett.* 140 (3), 167–171.
- Kassem, K.O., Hussein, M.A.T., Motawea, M.M., Gomaa, H., Alrowaili, Z.A., Ezzeldien, M., 2021. Design of mesoporous ZnO @ silica fume-derived SiO₂ nanocomposite as photocatalyst for efficient crystal violet removal: Effective route to recycle industrial waste. *J. Clean. Prod.* 326, 129416.
- Kulkarni, P., Nataraj, S.K., Balakrishna, R.G., Nagaraju, D.H., Reddy, M.V., 2017. Nanostructured binary and ternary metal sulfides: synthesis methods and their application in energy conversion and storage devices. *J. Mater. Chem. A* 5 (42), 22040–22094.
- Leach, A.D.P., Macdonald, J.E., 2016. Optoelectronic properties of CuInS₂ nanocrystals and their origin. *J. Phys. Chem. Lett.* 7 (3), 572–583.
- Li, S., Cai, M., Liu, Y., Zhang, J., Wang, C., Zang, S., Li, Y., Zhang, P., Li, X., 2022. In situ construction of a C₃N₅ nanosheet/Bi₂WO₆ nanodot S-scheme heterojunction with enhanced structural defects for the efficient photocatalytic removal of tetracycline and Cr(vi). *Inorg. Chem. Front.* 9 (11), 2479–2497.
- Li, K., Lu, X., Zhang, Y., Liu, K., Huang, Y., Liu, H., 2020. Bi₃TaO₇/Ti₃C₂ heterojunctions for enhanced photocatalytic removal of water-borne contaminants. *Environ. Res.* 185, 109409.
- Li, H., Yu, H., Chen, S., Zhao, H., Zhang, Y., Quan, X., 2014. Fabrication of graphene wrapped ZnIn₂S₄ microspheres heterojunction with enhanced interfacial contact and its improved photocatalytic performance. *Dalton Trans.* 43 (7), 2888–2894.
- Liang, J., Huang, X., Yan, J., Li, Y., Zhao, Z., Liu, Y., Ye, J., Wei, Y., 2021. A review of the formation of Cr(VI) via Cr(III) oxidation in soils and groundwater. *Sci. Total Environ.* 774, 145762.
- Lima, L.M., Silva, B.N.M.D., Barbosa, G., Barreiro, E.J., 2020. β-lactam antibiotics: An overview from a medicinal chemistry perspective. *Eur. J. Med. Chem.* 208.
- Ling, Z., Ren Chang, E., Zhao, M.-Q., Yang, J., Giammarco James, M., Qiu, J., Barsoum Michel, W., Gogotsi, Y., 2014. Flexible and conductive MXene films and nanocomposites with high capacitance. *Proc. Nat. Acad. Sci.* 111 (47), 16676–16681.
- Liu, Q., Tan, X., Wang, S., Ma, F., Znad, H., Shen, Z., Liu, L., Liu, S., 2019b. MXene as a non-metal charge mediator in 2D layered CdS@Ti₃C₂@TiO₂ composites with superior Z-scheme visible light-driven photocatalytic activity. *Environ. Sci. Nano* 6 (10), 3158–3169.
- Liu, T., Wang, C., Wang, W., Xu, P., Sun, X., Zhang, J., 2021. The enhanced performance of Cr(VI) photoreduction and antibiotic removal on 2D/3D TiO₂/ZnIn₂S₄ nanostructures. *Ceram. Int.* 47 (2), 17015–17022.
- Liu, Y., Zeng, H., Chai, Y., Yuan, R., Liu, H., 2019a. Ti₃C₂/BiVO₄ Schottky junction as a signal indicator for ultrasensitive photoelectrochemical detection of VEGF₁₆₅. *Chem. Commun.* 55 (91), 13729–13732.
- Lu, C., Guo, F., Yan, Q., Zhang, Z., Li, D., Wang, L., Zhou, Y., 2019. Hydrothermal synthesis of type II ZnIn₂S₄/BiPO₄ heterojunction photocatalyst with dandelion-like microflower structure for enhanced photocatalytic degradation of tetracycline under simulated solar light. *J. Alloy. Compd.* 811, 151976.
- Lukatskaya Maria, R., Mashtalir, O., Ren Chang, E., Dall’Agnese, Y., Rozier, P., Taberna Pierre, L., Naguib, M., Simon, P., Barsoum Michel, W., Gogotsi, Y., 2013. Cation intercalation and high volumetric capacitance of two-dimensional titanium carbide. *Science* 341(6153), 1502–1505.
- Luo, L., Dong, S., Chen, H., Jin, H., Huang, T., 2022. Construction of MgIn₂S₄/ZnIn₂S₄ micro-flowers: Efficient degradation of tetracycline hydrochloride over a wide pH range. *Appl. Surf. Sci.* 581, 152417.
- Meng, A., Zhang, L., Cheng, B., Yu, J., 2019. Dual cocatalysts in TiO₂ photocatalysis. *Adv. Mater.* 31 (30), 1807660.
- Micoine, K., Persich, P., Llaviera, J., Lam, M.-H., Maderna, A., Loganzo, F., Fürstner, A., 2013. Total syntheses and biological reassessment of lactimidomycin, isomigrastatin and congener glutarimide antibiotics. *Chem. – A Eur. J.* 19 (23), 7370–7383.
- Ou, M., Li, J., Chen, Y., Wan, S., Zhao, S., Wang, J., Wu, Y., Ye, C., Chen, Y., 2021. Formation of noble-metal-free 2D/2D ZnmIn₂S_{m+3} (m = 1, 2, 3)/MXene Schottky heterojunction as an efficient photocatalyst for hydrogen evolution. *Chem. Eng. J.* 424, 130170.
- Ouyang, C., Quan, X., Zhang, C., Pan, Y., Li, X., Hong, Z., Zhi, M., 2021. Direct Z-scheme ZnIn₂S₄@MoO₃ heterojunction for efficient photodegradation of tetracycline hydrochloride under visible light irradiation. *Chem. Eng. J.* 424, 130510.
- Peng, Y., Geng, M., Yu, J., Zhang, Y., Tian, F., Guo, Y.n., Zhang, D., Yang, X., Li, Z., Li, Z. and Zhang, S., 2021. Vacancy-induced 2H@1T MoS₂ phase-incorporation on ZnIn₂S₄ for boosting photocatalytic hydrogen evolution. *Appl. Catal. B: Environ.* 298, 120570.
- Peng, Y., Guo, X., Xu, S., Guo, Y.n., Zhang, D., Wang, M., Wei, G., Yang, X., Li, Z., Zhang, Y., Tian, F., 2022. Surface modulation of MoS₂/O-ZnIn₂S₄ to boost photocatalytic H₂ evolution. *J. Energy Chem.* 75, 276–284.
- Peng, Q., Guo, J., Zhang, Q., Xiang, J., Liu, B., Zhou, A., Liu, R., Tian, Y., 2014. Unique lead adsorption behavior of activated hydroxyl group in two-dimensional titanium carbide. *J. Am. Chem. Soc.* 136 (11), 4113–4116.
- Qiu, Z.-M., Bai, Y., Gao, Y.-D., Liu, C.-L., Ru, Y., Pi, Y.-C., Zhang, Y.-Z., Luo, Y.-S., Pang, H., 2022. MXenes nanocomposites for energy storage and conversion. *Rare Met.* 41 (4), 1101–1128.
- Qu, Y., Xu, X., Huang, R., Qi, W., Su, R., He, Z., 2020. Enhanced photocatalytic degradation of antibiotics in water over functionalized N, S-doped carbon quantum dots embedded ZnO nanoflowers under sunlight irradiation. *Chem. Eng. J.* 382, 123016.
- Raja, A., Son, N., Swaminathan, M., Kang, M., 2021. Facile synthesis of sphere-like structured ZnIn₂S₄-rGO-CuInS₂ ternary heterojunction catalyst for efficient visible-active photocatalytic hydrogen evolution. *J. Colloid Interface Sci.* 602, 669–679.
- Sahoo, G.C., Ghosh, A.C., Dutta, N.N., Mathur, R.K., 1996. Facilitated transport of 7-aminoccephalosporanic acid in a bulk liquid membrane. *J. Membr. Sci.* 112 (2), 147–154.
- Sun, W.-J., Zhao, Y.-Y., Cheng, X.-F., He, J.-H., Lu, J.-M., 2020. Surface functionalization of single-layered Ti₃C₂T_x mXene and its

- application in multilevel resistive memory. *ACS Appl. Mater. Interfaces* 12 (8), 9865–9871.
- Tan, H.L., Abdi, F.F., Ng, Y.H., 2019. Heterogeneous photocatalysts: an overview of classic and modern approaches for optical, electronic, and charge dynamics evaluation. *Chem. Soc. Rev.* 48 (5), 1255–1271.
- Tariq, A., Ali, S.I., Akinwande, D., Rizwan, S., 2018. Efficient visible-light photocatalysis of 2D-MXene nanohybrids with Gd^{3+} - and Sn^{4+} -codoped bismuth ferrite. *ACS Omega* 3 (10), 13828–13836.
- Wang, H., Peng, R., Hood, Z.D., Naguib, M., Adhikari, S.P., Wu, Z., 2016b. Titania composites with 2 D transition metal carbides as photocatalysts for hydrogen production under visible-light irradiation. *ChemSusChem* 9 (12), 1490–1497.
- Wang, Z., Wang, Y., Gu, Q., Zhao, C., Zhang, J., Xu, S., Lu, M., Zhang, B., 2023. Multi-ion intercalated $Ti_3C_2T_x$ MXene and the mutual modulation within interlayer. *Particuology* 72, 10–16.
- Wang, H., Wu, Y., Yuan, X., Zeng, G., Zhou, J., Wang, X., Chew, J. W., 2018. Clay-inspired MXene-based electrochemical devices and photo-electrocatalyst: State-of-the-art progresses and challenges. *Adv. Mater.* 30 (12), 1704561.
- Wang, T., Yang, Y., Deng, Q., Zhang, X., Xiong, L., Tang, Z., Li, P., Yin, N., Sun, A., Chen, D., Shen, J., 2021. In-situ construction of 3D marigold-like CoAl-LDH/ Ti_3C_2 heterosystem collaborating with 2D/2D interface for efficient photodegradation of multiple antibiotics. *Appl. Surf. Sci.* 569, 151084.
- Wang, H., Yuan, X., Wang, H., Chen, X., Wu, Z., Jiang, L., Xiong, W., Zeng, G., 2016a. Facile synthesis of Sb_2S_3 /ultrathin g- C_3N_4 sheets heterostructures embedded with g- C_3N_4 quantum dots with enhanced NIR-light photocatalytic performance. *Appl. Catal. B* 193, 36–46.
- Wu, Y., Wang, H., Tu, W., Liu, Y., Wu, S., Tan, Y.Z., Chew, J.W., 2018. Construction of hierarchical 2D–2D $Zn_3In_2S_6$ /fluorinated polymeric carbon nitride nanosheets photocatalyst for boosting photocatalytic degradation and hydrogen production performance. *Appl. Catal. B* 233, 58–69.
- Xiang, W., Wan, Y., Zhang, X., Tan, Z., Xia, T., Zheng, Y., Gao, B., 2020. Adsorption of tetracycline hydrochloride onto ball-milled biochar: Governing factors and mechanisms. *Chemosphere* 255, 127057.
- Xiao, T., Tang, Z., Yang, Y., Tang, L., Zhou, Y., Zou, Z., 2018. In situ construction of hierarchical $WO_3/g-C_3N_4$ composite hollow microspheres as a Z-scheme photocatalyst for the degradation of antibiotics. *Appl. Catal. B* 220, 417–428.
- Xiao, Y., Zhang, W., Xing, Q., Feng, X., Jiang, Y., Gao, Y., Xu, H., Zhang, J., Ni, L., Liu, Z., 2020. Eco-friendly synthesis of core/shell $ZnIn_2S_4/Ta_3N_5$ heterojunction for strengthened dual-functional photocatalytic performance. *Int. J. Hydrogen Energy* 45 (55), 30341–30356.
- Xu, H., Jiang, Y., Yang, X., Li, F., Li, A., Liu, Y., Zhang, J., Zhou, Z., Ni, L., 2018. Fabricating carbon quantum dots doped $ZnIn_2S_4$ nanoflower composites with broad spectrum and enhanced photocatalytic Tetracycline hydrochloride degradation. *Mater. Res. Bull.* 97, 158–168.
- Yan, M., Hua, Y., Zhu, F., Gu, W., Jiang, J., Shen, H., Shi, W., 2017. Fabrication of nitrogen doped graphene quantum dots-BiOI/ $MnNb_2O_6$ p-n junction photocatalysts with enhanced visible light efficiency in photocatalytic degradation of antibiotics. *Appl. Catal. B* 202, 518–527.
- Yang, Y., Zeng, Z., Zhang, C., Huang, D., Zeng, G., Xiao, R., Lai, C., Zhou, C., Guo, H., Xue, W., Cheng, M., Wang, W., Wang, J., 2018. Construction of iodine vacancy-rich BiOI/Ag@AgI Z-scheme heterojunction photocatalysts for visible-light-driven tetracycline degradation: Transformation pathways and mechanism insight. *Chem. Eng. J.* 349, 808–821.
- Yang, Y., Zeng, Z., Zeng, G., Huang, D., Xiao, R., Zhang, C., Zhou, C., Xiong, W., Wang, W., Cheng, M., Xue, W., Guo, H., Tang, X., He, D., 2019a. Ti_3C_2 MXene/porous g- C_3N_4 interfacial Schottky junction for boosting spatial charge separation in photocatalytic H_2O_2 production. *Appl. Catal. B* 258, 117956.
- Yang, Y., Wu, J., Xiao, T., Tang, Z., Shen, J., Li, H., Zhou, Y., Zou, Z., 2019b. Urchin-like hierarchical CoZnAl-LDH/RGO/g- C_3N_4 hybrid as a Z-scheme photocatalyst for efficient and selective CO_2 reduction. *Appl. Catal. B* 255, 117771.
- Ye, J., He, J., Wang, S., Zhou, X., Zhang, Y., Liu, G., Yang, Y., 2019. Nickel-loaded black TiO_2 with inverse opal structure for photocatalytic reduction of CO_2 under visible light. *Sep. Purif. Technol.* 220, 8–15.
- Yu, T., Wu, W., Liu, L., Gao, C., Yang, T., 2020. Novel ternary p- $ZnIn_2S_4/rGO/n-g-C_3N_4$ Z-scheme nanocatalyst with enhanced antibiotic degradation in a dark self-biased fuel cell. *Ceram. Int.* 46 (7), 9567–9574.
- Yuan, Y.-J., Tu, J.-R., Ye, Z.-J., Chen, D.-Q., Hu, B., Huang, Y.-W., Chen, T.-T., Cao, D.-P., Yu, Z.-T., Zou, Z.-G., 2016. MoS_2 -graphene/ $ZnIn_2S_4$ hierarchical microarchitectures with an electron transport bridge between light-harvesting semiconductor and cocatalyst: A highly efficient photocatalyst for solar hydrogen generation. *Appl. Catal. B* 188, 13–22.
- Zhang, S., Zhang, Z., Li, B., Dai, W., Si, Y., Yang, L., Luo, S., 2021. Hierarchical $Ag_3PO_4@ZnIn_2S_4$ nanoscoparium: An innovative Z-scheme photocatalyst for highly efficient and predictable tetracycline degradation. *J. Colloid Interface Sci.* 586, 708–718.
- Zhao, Y., Wang, Y., Liang, X., Shi, H., Wang, C., Fan, J., Hu, X., Liu, E., 2019. Enhanced photocatalytic activity of Ag-CsPbBr₃/CN composite for broad spectrum photocatalytic degradation of cephalosporin antibiotics 7-ACA. *Appl. Catal. B* 247, 57–69.